

Replies to Editor # Comments/Suggestions

Dear authors, please check the wording and also citations carefully. I have found the phrase 'well-known', e.g. page 11 line 262 but no citations. Please go through your manuscript and check if you backed all claims with citations. It has been a major criticism that you mixed up known results and results obtained by you.

Reply: First of all, we wish to thank the Editor for handling the manuscript and for offering his/her constructive comments/suggestions, which improved the manuscript content significantly. In the revised version, we have taken care of proper citation to previous and differentiated the results.

On page 11 line 275: what do you mean here? La Nina is a an atmospheric condition. How can El Nino extend over El Nina (I suppose you mean La Nina?)?

Reply: we have revised the this statement in the manuscript as 'During the La Niña, the anticyclone circulation extends large compared to El Niño years at 100 hPa as shown in the Figure 8a'

On page 8. The phrases 'good rainfall' and 'less rainfall' sound rather subjective. I think you should briefly summarize the definition of active and break days and not force the reader to study another paper.

Reply: we have added the detailed discussion about the definition of active and break in the revised version.

Once again, we would like to thank the Editor for his/her thoughtful comments and suggestions that led to substantial improvements in the revised manuscript.

---END---

Asian Summer Monsoon Anticyclone: Trends and Variability

Ghouse Basha¹, M. Venkat Ratnam¹ and Pangaluru Kishore²

¹National Atmospheric Research Laboratory, Department of Space, Gadanki-517112, India.

² Department of Earth System Science, University of California, Irvine, CA, 92697, USA.

Correspondence to: Ghouse Basha (mdbasha@narl.gov.in)

Abstract

The Asian Summer Monsoon Anticyclone (ASMA) has been a topic of intensive research in recent times through its variability in dynamics, chemistry and radiation. This work explores the spatial variability and the trends of the ASMA using observational and

42 reanalysis data sets. Our analysis indicates that the spatial extent and magnitude of ASMA is
43 greater during July and August compared to June and September. The decadal variability of
44 the anticyclone is very large at the edges of the anticyclone than at the core region.
45 Significant decadal variability is observed in the northeast and southwest parts of ASMA
46 with reference to the 1951-1960 period. The strength of the ASMA shows a drastic increase
47 in zonal wind anomalies in terms of temporal variation. Further, our results show that the
48 extent of the anticyclone is greater during the active phase of the monsoon, strong monsoon
49 years, and La Niña events. Significant warming with strong westerlies is observed exactly
50 over the Tibetan Plateau from the surface to tropopause during the active phase of the
51 monsoon, strong monsoon years, and during La Niña events. Our results support the transport
52 process over Tibetan Plateau and the Indian region during active, strong monsoon years and
53 during strong La Niña years. It is suggested to consider different phases of monsoon while
54 interpreting the variability of pollutants/trace gases in the anticyclone.

55 *Keywords:* Asian Monsoon, anticyclone, geopotential height, La Niña, El Niño, and rainfall.

Deleted: Niño

56

57

58

59

60

61

62

63

64

65

66

1. Introduction

The Asian Summer Monsoon Anticyclone (ASMA) is a dominant circulation in the Northern Hemisphere (NH) summer in the Upper Troposphere and Lower Stratosphere (UTLS), which extends from Asia to the Middle East. ASMA is bordered by the subtropical westerly jet in the north and easterly jets to the south. The Asian Summer Monsoon (ASM) dynamics act as a pathway for the transport of trace gases and pollutants both vertically (through convection) and horizontally (through low-level jet and tropical easterly jet). The ASMA circulation responds to heating corresponding to the deep convection of the south

68 Asian monsoon (Hoskins and Rodwell, 1995; Highwood and Hoskins, 1998). This strong
69 anticyclone circulation isolates the air and is tied to the outflow of deep convection, which
70 has distinct maximum characteristics in terms of dynamical and chemical variability (Randel
71 and Park, 2006; Park et al., 2007). Recently, the anticyclone circulation in UTLS has been
72 paid more attention by researchers in order to understand the dynamics, chemistry, and
73 radiation of the region. This problem has been discussed by several authors (e.g., Park et al.,
74 2007; Fadnavis et al., 2014; Glatthor et al., 2015; Vernier et al., 2015; Santee et al., 2017).
75 Deep convection during monsoon can transport tropospheric tracers from the surface to the
76 UTLS (Vogel et al., 2015; Tissier and Legras, 2016). The tracers which are transported are
77 confined in the anticyclone will affect the trace gas concentration in the UTLS resulting in
78 significant changes in radiative forcings (Solomon et al., 2010; Riese et al., 2012; Hossaini et
79 al., 2015). The center of the anticyclone is located either over the Iranian Plateau or over the
80 Tibetan Plateau where the distribution of pollutants and tracers vary significantly (Yan et al.,
81 2011).

82 The spatial extent, strength, and the location of an anticyclone vary on several
83 temporal scales caused by internal dynamical variability of the Asian monsoon (Zhang et al.,
84 2002; Randel and Park, 2006; Garny and Randel, 2013; Vogel et al., 2015; Pan et al., 2016).
85 However, the variability of the anticyclone structure and response to Indian monsoon activity
86 are not understood. Further, the tracers (O₃, and CO etc.) trapped in the anticyclone during
87 the same period in the UTLS region. Since the anticyclone extends from the Middle East to
88 East Asia, trapped pollutants are expected to make a large radiative forcing to the background
89 atmosphere. Thus, it is essential to understand the variability of anticyclone structure itself in
90 detail and its response to Indian Summer Monsoon (ISM). Therefore, in the first part of the
91 study, we investigate the spatial, inter-annual and decadal variations of the anticyclone. Since
92 the Indian monsoon responds at different time scales, we also investigated the anticyclone

variability with respect to the active and break spells of the Indian monsoon, strong and weak monsoon years, and the stronger El Nino Southern Oscillation (ENSO) years. For this, we have utilized the NCEP/NCAR reanalysis geopotential height from 1951 to 2016. The structure of the paper is as follows. We describe the data sets used in this study in Section 2. Section 3 contains the seasonal and decadal variation of the anticyclone. Section 4 shows the influence of ISM on anticyclone i.e. active and break spells, strong and weak monsoon years, and ENSO's effects on the anticyclone. Finally, we discuss our results presented in Section 5.

2. Data and Methodology

2.1. NCEP/NCAR Reanalysis

The National Center for Environmental Prediction (NCEP), in collaboration with the National Center for Atmospheric Research (NCAR) produces reanalysis data from a consistent assimilation and modeling procedure that incorporates all the available observed conditions obtained from conventional and satellite information from 1951 to the present (Kalnay et al. 1996). We used NCEP/NCAR reanalysis daily geopotential height (GPH) and wind data from the years 1951 to 2016. The NCEP/NCAR data assimilation uses a 3D-variational analysis scheme with 28 pressure levels and triangular truncation of 62 waves (horizontal resolution of 200m). Both GPH and temperature at the chosen standard levels are described as class output variables (Kalnay et al. 1996) i.e. they are strongly influenced by observed data. Only the Indian summer monsoon months (June, July, and August, September) containing gridded daily data were considered in this study. The NCEP/NCAR reanalysis data had a spatial resolution of 2.5° . The seasonal values are estimated from daily data. To identify the spatial and temporal variations of the anticyclone center, we used the monthly mean values of the GPH and the zonal wind component. The quality of NCEP GPH reanalysis data can be found from Bromwich et al. (2007).

2.2. IMD Gridded Precipitation Data

118 The India Meteorological Department (IMD) high-resolution (0.25°x0.25°) gridded
119 precipitation data is used to identify the active and break spells during June, July and August
120 months from 1951-2016 (Pai et al. 2016). This precipitation data has been validated
121 extensively with observational and reanalysis data sets and displays a very good correlation
122 (Kishore et al., 2016). Data from 1951-2016 have been used. We have identified the active
123 and break spells based on daily rainfall over monsoon core zone of India (which is roughly
124 from 18°N to 28°N and 65°E to 88°E) during July and August months as reported by
125 Rajeevan et al. (2010). The **normalized** anomaly is estimated from the averaged daily rainfall
126 in the monsoon core zone is subtracted from its long term (1951-2000) mean and by dividing
127 with its daily standard deviation. The active (break) spells were identified from the
128 **normalized** anomaly when rainfall is greater (lesser) than -1.0 (+1.0), consecutively for three
129 days or more. Data from 1951-2016 have been used.

130 2.3. GNSS Radio Occultation (RO) Data

131 We have also used the Global Navigation Satellite System (GNSS) Radio Occultation
132 (RO) data for investigating the temperature anomaly. The basic measurement principle of RO
133 exploits the atmosphere-induced phase delay in the GNSS signals, which are recorded in the
134 low earth-orbiting satellite. This technique provides vertical profiles of refractivity, density,
135 pressure, temperature, and water vapor (Kursinski et al., 1997). The temperature profiles
136 from this technique are available with low horizontal (~200-300 km) and high vertical
137 resolutions (10-35 km) with an accuracy of <0.5 K. We used the CHALLENGING Minisatellite
138 Payload (CHAMP) and Constellation Observing System for Meteorology, Ionosphere, and
139 Climate (COSMIC) covering the period from 2002 to 2016.

140 The CHAMP satellite was launched on 15 July 2000 into a circular orbit by Germany
141 to measure the Earth's gravity and magnetic field and to provide global RO soundings
142 (Wickert et al. 2001). About ~230 RO profiles per day were measured by the CHAMP

Deleted:). For identification of active (or wet) and break (or dry) spells, we followed a similar procedure as described by Rajeevan et al. (2010) and Pai et al. (2016) over the monsoon core zone (18°N-28°N, and 65°E-88°E).

Deleted: normalised

Deleted: the

Deleted: normalised

Deleted: .

151 payload since 2002. The CHAMP payload was solely designed to track the setting
152 occultations, and the RO event gets terminated when the signal is lost, which results in a
153 decrease in the number of occultations with a decreasing altitude (Beyerle et al. 2006). This
154 receiver measures the phase delay of radio wave signals that are occulted by the Earth's
155 atmosphere. From this phase delay, it is possible to retrieve the bending angle and refractivity
156 vertical profiles.

157 COSMIC consists of a constellation of 6 satellites, which was launched in April 2006
158 to a circular, 72° inclination orbit at a 512 km altitude capable of receiving signals from the
159 Global Positioning System (GPS) (Anthes et al., 2008). Compared to previous satellites,
160 COSMIC satellites employed an open loop mode, which can track both the rising and setting
161 of occultations (Schreiner et al. 2007). The open-loop tracking technique significantly
162 reduces the GPS RO inversion biases by eliminating tracking errors (Sokolovskiy et al.
163 2006). The COSMIC temperature profiles display a very good agreement with radiosonde
164 data, reanalyses, and models (Rao et al., 2009; Kishore et al., 2011; Kishore et al., 2016). The
165 CHAMP and COSMIC GPSRO data was interpolated to 200 m from their native resolution.
166 We derived the cold point tropopause altitude/temperature over the ASMA region as
167 discussed by Ratnam et al. (2014) and Ravindrababu et al. (2015). Both the CHAMP and
168 COSMIC data were obtained from COSMIC Data Analysis and Archive Center (CDAAC)
169 (<https://cdaac-www.cosmic.ucar.edu/cdaac/products.html>).

170 **3. Results and Discussion**

171 **3.1. Variability of the Anticyclone**

172 The climatological spatial variability of the GPH and wind vectors at 100 hPa during
173 June, July, August and September months from NCEP reanalysis data is shown in Figure 1(a,
174 b, c & d). The anticyclone circulation is clearly depicted during June, July, August, and
175 September by wind vectors (Figure 1). During the month of September and June, the values

of GPH are low compared to July and August which represents the spatial extent of the anticyclone. The spatial extent and intensity of the anticyclone are greater during July compared to the other months. During July and August, the anticyclone extends from East Asia to the Middle East. The spatial extent of the anticyclone circulation is clearly evident in the grid 15°N-45°N; 30°E-120°E at 100 hPa level and the climatological averaged values of GPH varies from 16.5-17 km in NCEP reanalysis during 1951-2016. Using the modified potential vorticity equation, Randel et al. (2006) showed the spatial variation of the anticyclone where GPH values are stationary in the range of 16.75-16.9 km. Similarly, Park et al. (2007) showed the anticyclone structure from the strongest wind at 100 hPa through streamline function. Bian et al. (2012) reported the spatial variability of the anticyclone using 16.77 km and 16.90 km in the GPH contour as the lower and the upper boundary, respectively. Thus, these empirically selected GPH values represent the anticyclone boundaries. Therefore, in this present study, we have chosen the values from 16.75 to 16.9 km to investigate the spatial features of the anticyclone and the resultant picture is depicted in Figure 1(e, f, g & h). The spatial extent and existence of the anticyclone are highly prominent during July and August compared to June. During the September month, very low values of GPH are seen compared to July and August. Therefore, we considered the average of July and August GPH from 1951-2016 for further analysis as shown in Figure S1. The core region and the spatial extent of the anticyclone are clearly evident from Figure S1. The core region of the anticyclone shows bimodal distribution i.e. one core located at the south-western flank of the Himalayas and another over Iran. The core region over the south-western flank of Himalayas is due to large scale updraft, which is caused by the moist energy over Indo-Gangetic plain, heating of Tibetan plateau, and the orographic forcing of the Himalayas. Severe heating over Arabian Peninsula supports the formation of the mid-tropospheric the anticyclone in the west. This anticyclone can merge intermittently within ASMA. It is also

201 observed that the spatial extent of the anticyclone varies drastically at different temporal
202 scales. Therefore, seasonal variation is much more pronounced.

203 The decadal variation of the anticyclone is studied with respect to the spatial
204 variability. Figure 2 shows the decadal spatial variation of the anticyclone with reference to
205 the years 1951-1960. The significant difference in the decadal variation is noticed in Figure 2.
206 The edges (east, north, and west) of the anticyclone undergo drastic changes during the
207 period 1961-1970. In case of 1971-1980 period, except for a small portion in the east, the
208 whole anticyclone shows drastic changes. During the decade 1971-1980, the recorded GPH
209 values in the anticyclone are lower by ~ 25 m when compared to the values in 1951-1960.
210 This feature is quite opposite during 1981-1990 where high values (~ 30 m) are observed
211 compared to those in the reference period. The GPH difference is significant over the west,
212 northeast and southern regions of the anticyclone during the 1991-2000 period. Similar
213 changes are observed during 2001-2010. Compared to all the decadal differences, 2011-2016
214 shows a completely different picture. The changes are only in the western and north-eastern
215 corner, whereas other parts of the anticyclone do not show any change. From this analysis,
216 we observed significant changes in the anticyclone even from one decade to another, which
217 can result in a change in chemical and dynamical changes over this region.

218 Further, the spatial distribution of trend is estimated during the years 1951-2016 by
219 using robust regression analysis at 95% confidence interval as displayed in Figure 3. The
220 edges on all sides of the anticyclone undergo noticeable changes compared to the core region.
221 The east and north-west side of the anticyclone shows an increasing trend compared to other
222 regions. The trends at the northern end are significant than the southern end. A few portions
223 on the northern side of the anticyclone show a reduction in the strength. Therefore, in order to
224 understand the asymmetry in the anticyclone variability, we have divided the anticyclone
225 region into 4 different sectors as shown in Figure 4 based on the peak values of GPH along

Deleted: .

Formatted: Font color: Auto

227 longitude and latitude cross-sections. The center values of GPH are located at 70°E longitude
228 and 32.5°N Latitude. The four sectors can be divided into South-East (SE) (22.5°N-32.5°N),
229 North-East (NE) (32.5°N-40°N) in the longitude band of 70°E-120°E, South-West (SW)
230 (22.5°N-32.5°N), and North-West (NW) (32.5°N-40°N) at the 20°E-70°E longitude range.
231 The area-averaged time series (July and August) of zonal wind anomalies in these sectors
232 from 1951-2016 are shown in Figure 5. The zonal wind anomalies show a clearly increasing
233 trend in all the sectors. From the year 1951 to 1980, the zonal wind anomalies are negative
234 and shift to positive in all the sectors. The year 1980 represents the beginning of
235 industrialization globally (Basha et al., 2017). The change is highly significant in the north-
236 west and north-east sectors with a magnitude variability of 7.59 m/s from 1951-2016 whereas
237 it is 5.44 m/s in the south-east and south-west sectors. In addition, we estimated the strength
238 of the anticyclone during the monsoon season by using a difference in the zonal wind
239 between the northern (30°N-40°N) and southern (10°N-20°N) flanks of the anticyclone,
240 which is depicted in Figure 5e. A significant increase in the strength of the anticyclone is
241 noticed from Figure 5e at a rate of 0.157 m/s per year (10.36 m/s from 1951-2016).

242 It is well known that the Indian monsoon rainfall varies at different time scales i.e.
243 daily, sub-seasonal, interannual, decadal and centennial scales (Rajeevan et al., 2010).
244 Precipitation during the monsoon varies from intra-seasonal scales between active (good
245 rainfall) and break (less rainfall) spells. Any small change in the precipitation pattern will
246 affect the anticyclone due to the thermodynamics involved in rainfall. In this study, we also
247 investigated the anticyclone variability during the active and break spells of the Indian
248 monsoon. The active and break spells were identified in July and August by using the high
249 resolution gridded (0.25° x 0.25°) rainfall data from 1951 to 2016 as defined by Pai et al.
250 (2016).

Deleted: 0

252 The number of active and break days is derived from the precipitation data shown in
253 Figure S2 (a & b). Daily GPH, temperature, and zonal wind are taken from NCEP reanalysis
254 whereas the tropopause altitude is derived from the GNSS RO data for active and break days.
255 The anticyclone structure during active (red line) and break (blue line) days are shown in
256 Figure 6a. Two interesting aspects of the anticyclone variability can be noticed between
257 active and break days. One aspect is the extent of the anticyclone is large during active days
258 compared to break days and another is the existence of two cell structures in the anticyclone
259 core region during active days. The extent is large in the eastern and northern side in active
260 days. The zonal (meridional) cross-section of temperature (color shade), zonal wind (contour
261 lines) difference between active and break phase averaged in the longitude band of 80°E-90°E
262 (latitude band of 30°N-40°N) along with cold point tropopause for active and break days is
263 illustrated in Figures 6b & 6c. During active days, temperature shows cooling in tropical
264 latitudes whereas it shows warming in the mid-latitudes from surface to the tropopause.
265 Significant warming is observed during the active days in the mid-troposphere over the
266 Tibetan Plateau and its northern side. Westerly (easterly) winds exist over the cooler
267 (warmer) regions. The warm temperature anomalies stretch from 1.5 to 12 km in between
268 25°N and 60°N. The tropopause altitude is low (high) during the active (break) phase of
269 Indian monsoon as shown in Figure 6b. The meridional cross-section of temperature
270 anomalies displays significant warming from ~1.5 to 8 km over the Indian region. The
271 tropopause altitude exemplifies random variability in the meridional cross-section.

272 As discussed previously, the anticyclone circulation is significant during the months
273 of July and August when most of the precipitation occurs over India (Basha et al., 2013;
274 Basha et al., 2015; Kishore et al., 2015; Narendra Reddy et al., 2018). The influence of strong
275 and weak monsoon years will have a drastic impact on anticyclone circulation. In order to
276 understand these changes, we have divided the years into strong and weak monsoon years

277 based on gridded precipitation data over the domain 5°N-30°N and 70°E-95°E from the years
278 1951-2016. This region is known to have heavy precipitation and orographic forcing, which
279 helps transport of water vapor through deep convection to UTLS (Houze et al., 2007; Medina
280 et al., 2010; Pan et al., 2016). The detrended precipitation represents the strong and weak
281 monsoon years. Years with positive (negative) values of precipitation shows the strong
282 (weak) monsoon years as shown in Figure S2b. The composite of mean distribution of the
283 anticyclone circulation during strong and weak monsoon years is shown in Figure 7a based
284 on GPH values at 100 hPa from NCEP reanalysis data. The circulation expands on the eastern
285 and western sides of the anticyclone during the strong monsoon years (red line). The core of
286 the anticyclone is significant during strong monsoon years. Clear eye structure is observed in
287 the core of the anticyclone on left (right) during the strong (weak) monsoon years. The
288 composite mean difference of temperature and zonal wind between the strong and weak
289 monsoon years along with tropopause altitude averaged in the longitude range of 80-85°E is
290 shown in Figure 7b. The warmest temperature anomalies are observed over the Tibetan
291 Plateau. Positive (warm) temperature anomalies exactly above the Tibetan Plateau (11 km)
292 and negative (cooling) on both sides are noticed in the lower troposphere from Figure 7b.
293 Strong easterlies (westerlies) winds are observed on the left (right) side of the Tibetan
294 Plateau. The whole Tibetan Plateau acts as a barrier that drives the cold air to upper altitudes
295 during strong monsoon years. Strong anticyclone circulation with strong westerlies at 35°N
296 and easterlies on both sides with elevated tropopause represent the impacts of the strong
297 monsoon vertically above the anticyclone. The rising motion over East Asia is excited by the
298 local heating of the Tibetan Plateau links to the single stretch vertically. The longitude and
299 altitude cross-section of temperature and wind anomalies shown in Figure 7c are averaged
300 between a latitude band of 35-40°N. Positive temperature anomalies are observed from the
301 surface to 12 km in the longitudes 60-80°E and stretch towards the west. This process clearly

302 demonstrates that a large scale ascent develops over the Asian monsoon region. The
303 tropopause altitude is high (low) during strong vertical motion and heavy precipitation is
304 noticed over the region similar to that reported by Lau et al. (2018). The transport processes
305 from the boundary layer to the tropopause occur on the east side of the anticyclone i.e.
306 southern flank of Tibetan Plateau, northeast India and the head of the Bay of Bengal. This
307 result is consistent with the previous studies by Bergman et al. (2013).

Deleted:

308 ENSO typically shows the strongest signal in boreal winter, but it can affect the
309 atmospheric circulation and constituent distributions until the next autumn (McPhaden et al.,
310 2006). It is well-known that strong ENSO events have a significant influence on tropical
311 upwelling and STE (Yan et al., 2018). This change can impact the distribution of the
312 composition and structure of the UTLS region. In the UTLS region, the tropopause responds
313 to the annual and interannual variability associated with ENSO (Trenberth, 1990) and QBO
314 (Baldwin et al., 2001). Several studies have been focused on the effects of the different
315 impacts of El Niño on tropopause and lower stratosphere (Hu and Pan, 2009; Zubiaurre and
316 Calvo, 2012; Xie et al., 2012). In the present study, we have investigated the changes
317 associated with strong ENSO events with the anticyclone circulation and tropical upwelling
318 during July and August. Therefore, we have also separated the GPH for the strongest El Niño
319 (1958, 1966, 1973, 1983, 1988, 1992, 1998, and 2015) and La Niña (1974, 1976, 1989, 1999,
320 2000, 2008, and 2011) years to verify the change in the circulation pattern of the anticyclone.

Deleted:

321 For this, we have chosen July and August GPH data at 100hPa as shown in Figure 8. The red
322 and blue colors indicate the composite of the La Niña and El Niño circulation. During the La
323 Niña, the anticyclone circulation extends large compared to El Niño years at 100 hPa as
324 shown in the Figure 8a. On the eastern and southern sides of the anticyclone, the expansion is
325 more during the La Niña years. The warm temperature with strong westerlies in the latitude
326 band of 43°N-55°N is observed during La Niña as shown in Figure 8b (Lau et al., 2018). The

Deleted: Niño

Deleted: is stronger and extends over the El Niña at

Deleted:

Deleted: Niño

cooling impact is significant over the Tibetan Plateau during La Niña events compared to El Niño events. Significant cooling is observed over the Tibetan Plateau and distributes towards tropical latitudes between 600-100 hPa. The zonal wind shows a convergence of easterly winds over the Tibetan Plateau from the mid to the upper tropospheric region. On the right side of the Tibetan Plateau there exist strong westerly winds from the surface to the tropopause altitudes with strong warming. The meridional cross-section of temperature and the zonal wind difference between La Niña and El Niño is shown in Figure 8c. Significant cooling is observed during La Niña in the longitude band of 80°E-100°E with strong easterlies from the surface to the tropopause. From this analysis, it is clear that the Indian summer monsoon variability has a significant impact on ASMA, and it is necessary to consider the different phases of monsoon while dealing with UTLS pollutants. In addition, we have investigated the zonal mean vertical cross-section in the longitude band of 50-60°E, which represents the Iranian Mode. Figure S3 depicts the difference between active and break phases, strong and weak monsoon years, and La Niña and El Niño years along with the tropopause altitude. Significant warming is observed during La Niña years and strong monsoon years compared to the active phase of the Indian monsoon in the troposphere. Compared to the Tibetan mode, Iranian mode warming is less. The tropopause altitude is slightly higher during the active phase of the Indian monsoon, strong monsoon years and La Niña years. A moderate increase in tropopause from the equator to 40°N is observed and decreases drastically afterward.

4. Summary and Conclusions

Several authors discussed the interannual and decadal variability of pollutants and tracers in the ASMA region from the model, observational and reanalysis data sets (Kunze et al., 2016; Santee et al., 2017; Yuan et al., 2019). In this present study, we have investigated the spatial variability, trends of the anticyclone and the influence of Indian monsoon activity i.e.

Deleted: Niño

active and break days, strong and weak monsoon years, and strong La Niña and El Niño years on ASMA using long-term reanalysis, satellite and observational data sets that were not investigated earlier. In this study, we have considered the GPH values from 16.75 km to 16.9 km, which represents the spatial structure of the anticyclone at 100 hPa. Our analysis shows that the spatial extent (magnitude) of the anticyclone structure is very large (strong) during July followed by August whereas it is very weak in June at 100 hPa. The bimodal distribution (Tibetan and Iranian modes) of the anticyclone is clearly observed during the month of July which is absent during other months (June and August). The anticyclone variability undergoes significant decadal variations from one decade to another. The edges of ASMA changes drastically compared to the core of the anticyclone. However, there are significant spatial differences in the structure of the anticyclone at 100 hPa. The anticyclone undergoes a decreasing trend on the northern side whereas an increasing trend on the western part. A significant increasing trend is observed in the spatially averaged zonal wind in four different sectors (Figure 5). The zonal wind anomalies show increasing trend in all the sectors at 100 hPa. The change is significant in the north-western and north-eastern sectors with a magnitude variability of 7.59 m/s from 1951-2016 whereas it is 5.44 m/s in the south-eastern and south-western sectors. The strength of the anticyclone increases with a rate of 0.157 m/s per year (10.36 m/s from 1951-2016) in the anticyclone region (Figure 5e). Yuan et al. (2019) also reported the increasing trend in the strength of the anticyclone by considering the MERRA 2 reanalysis data from 2001-2015.

Further, we have investigated the Indian monsoon influence on the anticyclone region. Our results reveal that the spatial extent of the anticyclone expands during the active phase of the Indian monsoon, the strong monsoon years and during strong La Niña years on the northern and eastern sides. A similar expansion of the anticyclone is noticed during strong monsoon years from MERRA2 data by Yuan et al. (2019). However, the ASMA boundaries

are not always well defined in all the events. The zonal mean cross-section of temperature shows significant warming over the Tibetan Plateau and from the surface to 12 km during the active phase of the Indian monsoon, the strong monsoon years, and the strong La Niña years. Similarly, the rise of tropopause during the active phase of the Indian monsoon, the strong monsoon years and the strong La Niña years are noticed. Since the Tibetan Plateau acts as a strong heat source in summer with the strongest heating layer lying in the lower layers, the thermal adaptation results in a shallow and weak cyclonic circulation near the surface, and a deep and strong anti-cyclonic circulation above it. During summer, the Tibetan Plateau acts as a strong heat source, which influences the whole UTLS region. The warm ascending air above will pull the air from below; the surrounding air in the lower troposphere converges towards the Tibetan Plateau area and climbs up the heating sloping surfaces (Bergman et al., 2013; Garny and Randel, 2016). Significant warming is observed over the Tibetan Plateau, which represents the strong transport of pollutants into the tropopause during the active phase of the Indian monsoon, the strong monsoon years, and the strong La Niña years. Pan et al. (2016) reported the transport of carbon monoxide through the southern flank of the Tibetan Plateau from the model analysis. The above-mentioned results indicate that the high mountain regions play a significant role in elevated heat sources during the formation and maintenance of the anticyclones over Asia. It emphasizes the role of the thermal forcing of the Tibetan Plateau on the temporal and the spatial evolution of the South Asian High. Lau et al. (2018) showed that the transport of the dust and pollutants from the Himalayas-Gangetic Plain and the Sichuan Basin.

Overall, we demonstrate the ASMA variability during different phases of the Indian monsoon. The uplifting of boundary layer pollutants to the tropopause level occurs primarily on the eastern side of the anticyclone, centered near the southern flank of the Tibetan Plateau, north-eastern India, Nepal, and north of the Bay of Bengal. The variability of tropopause

409 altitude and temperature, trace gases (Water Vapour (WV), Ozone (O₃), Carbon Monoxide
410 (CO) and aerosols (Attenuated Scattering Ratio (ASR) shows distinct in picture in ASMA
411 region. The ASMA itself is highly dynamical in nature and the confinement of tracers and
412 aerosols results in changes in its chemistry and radiation (Basha et al., 2019) However, a
413 more detailed and higher quality of the dataset is needed to further understand the effects of
414 the Tibetan Plateau on the transport of different tracers and pollutants to the UTLS region
415 (Ravindrababu et al., 2019).

416
417 *Data Availability.* The NCEP/NCAR reanalysis data are available from NOAA website
418 (<https://www.esrl.noaa.gov/psd/data/gridded/data.ncep.reanalysis.pressure.html>). The
419 COSMIC and CHAMP data is available from COSMIC CDAAC website. IMD gridded
420 precipitation data is available at National Climate data center Pune, India. All the data used in
421 the present study is available freely from the respective websites.

422 *Authors' Contributions.* GB and MVR conceived and designed the scientific questions
423 investigated in the study. GB performed the analysis and wrote the draft in close association
424 with MVR. PK estimated the active and break spells of the Indian monsoon. All authors
425 edited the paper.

426 *Competing Interests.* The authors declare that they have no competing financial interests.

427 *Acknowledgements.* We thank NCEP/NCAR reanalysis for providing reanalysis data. We
428 thank CDAAC for production of COSMIC and CHAMP GPSRO data and IMD gridded
429 precipitation data from National Climate data center Pune, India. This work was supported by
430 National Atmospheric Research Laboratory, Department of Space, and India

431 References

432 Anthes, R. A., Bernhardt, P. A., Chen, Y., Cucurull, L., Dymond, K. F., Ector, D., Healy, S.
433 B., Ho, S.-H., Hunt, D. C., Kuo, Y.-H., Liu, H., Manning, K., McCormick, C., Meehan, T.
434 K., Randel, W. J., Rocken, C., Schreiner, W. S., Sokolovskiy, S. V., Syndergaard, S.,

Deleted: association with

436 Thompson, D. C., Trenberth, K. E., Wee, T.-K., Yen, N. L., and Zeng, Z.: The
 437 COSMIC/Formosat/3 mission: Early results, *B. Am. Meteorol. Soc.*, 89, 313–333, 2008.
 438 Rao, D. N., Ratnam, M. V., Mehta, S., Nath, D., Ghouse Basha, S., Jagannadha Rao, V. V.
 439 M., Krishna Murthy, B. V., Tsuda, T., and Nakamura, K.: Validation of the COSMIC
 440 radio occultation data over Gadanki (13.48 N, 79.2 E): A tropical region, *Terr. Atmos.*
 441 *Ocean. Sci.*, 20, 59–70, doi:10.3319/TAO.2008.01.23.01(F3C), 2009.
 442 Baldwin, M. P., Gray, L. J., Dunkerton, T. J., Hamilton, K., Haynes, P. H., Randel, W. J.,
 443 Holton, J. R., Alexander, M. J., Hirota, I., Horinouchi, T., Jones, D. B. A., Kinnnersley, J.
 444 S., Marquardt, C., Sato, K., and Takahashi, M.: The quasi-biennial oscillation, *Rev.*
 445 *Geophys.*, 39, 179–229, doi:10.1029/1999RG000073, 2001.
 446 Basha, G., Kishore, P., Ratnam, M.V., Ouarda, T.B.M.J., Velicogna, I., and Tyler sutterly.:
 447 Vertical and latitudinal variation of the intertropical convergence zone derived using GPS
 448 radio occultation measurements, *Remote Sensing of Environment*,
 449 <http://dx.doi.org/10.1016/j.rse.2015.03.024>, 2015.
 450 Basha, G. and Ratnam, M. V.: Moisture variability over Indian monsoon regions observed
 451 using high resolution radiosonde measurements, *Atmos. Res.*, 132–133, 35–45,
 452 <https://doi.org/10.1016/j.atmosres.2013.04.004>, 2013.
 453 Basha, G., Kishore, P., Ratnam, M. V., Jayaraman, A., Kouchak, A. A., and Taha, B.J. M.:
 454 Historical and projected surface temperature over India during the 20th and 21st century.
 455 *Scientific Reports*, 7(1), 2987. <https://doi.org/10.1038/s41598-017-02130-3>, 2017.
 456 Basha, G., Ratnam, M. V., Kishore, P., Ravindrababu, S., and Velicogna, I.: Influence of
 457 Asian Summer Monsoon Anticyclone on the Trace gases and Aerosols over Indian region,
 458 *Atmos. Chem. Phys. Discuss.*, <https://doi.org/10.5194/acp-2019-743>, in review, 2019.

459 Bergman, J. W., Fierli, F., Jensen, E. J., Honomichl, S., and Pan, L. L.: Boundary layer
 460 sources for the Asian anticyclone: Regional contributions to a vertical conduit, *J. Geophys.*
 461 *Res.*, 118, 2560–2575, <https://doi.org/10.1002/jgrd.50142>, 2013.

462 Beyerle, G., Schmidt, T., Wickert, J., Heise, S., Rotacher, M., Koenig-Langlo, G., and
 463 Lauritsen, K. B.: Observations and simulations of receiver-induced refractivity biases in
 464 GPS radio occultation, *J. Geophys. Res.*, 111, D12101, doi:10.1029/2005JD006673, 2006.

465 Bian, J., Pan, L. L., Paulik, L., Vömel, H., and Chen, H.: In situ water vapor and ozone
 466 measurements in Lhasa and Kunmin during the Asian summer monsoon, *Geophys. Res.*
 467 *Lett.*, 39, L19808, doi:10.1029/2012GL052996, 2012.

468 Bromwich, D. H., Fogt, R. L., Hodges, K. I., and Walsh, J. E.: A tropospheric assessment of
 469 the ERA-40, NCEP, and JRA-25 global reanalyses in the polar regions, *J. Geophys. Res.-*
 470 *Atmos.*, 112, D10111, doi:10.1029/2006JD007859, 2007.

471 Fadnavis, S., Schultz, M. G., Semeniuk, K., Mahajan, A. S., Pozzoli, L., Sonbawne, S.,
 472 Ghude, S. D., Kiefer, M., and Eckert, E.: Trends in peroxyacetyl nitrate (PAN) in the
 473 upper troposphere and lower stratosphere over southern Asia during the summer monsoon
 474 season: regional impacts, *Atmos. Chem. Phys.*, 14, 12 725–12 743,
 475 <https://doi.org/10.5194/acp-14-12725-2014>, 2014.

476 Garny, H. and Randel, W. J.: Dynamic variability of the Asian monsoon anticyclone
 477 observed in potential vorticity and correlations with 5 tracer distributions, *J. Geophys.*
 478 *Res.*, 118, 13 421–13 433, <https://doi.org/10.1002/2013JD020908>, 2013.

479 Garny, H. and Randel, W. J.: Transport pathways from the Asian monsoon anticyclone to the
 480 stratosphere, *Atmos. Chem. Phys.*, 16, 2703-2718, [https://doi.org/10.5194/acp-16-2703-](https://doi.org/10.5194/acp-16-2703-2016)
 481 2016, 2016.

482 Glatthor, N., Höpfner, M., Stiller, G. P., von Clarmann, T., Funke, B., Lossow, S., Eckert, E.,
 483 Grabowski, U., Kellmann, S., Linden, A., Walker, K. A., and Wiegeler, A.: Seasonal and

484 interannual variations in HCN amounts in the upper troposphere and lower stratosphere
 485 observed by MIPAS, *Atmos. Chem. Phys.*, 15, 563–582, [https://doi.org/10.5194/acp-15-](https://doi.org/10.5194/acp-15-563-2015)
 486 563-2015, 2015.

487 Gottschaldt, K.-D., Schlager, H., Baumann, R., Cai, D. S., Eyring, V., Graf, P., Grewe, V.,
 488 Jöckel, P., Jurkat-Witschas, T., Voigt, C., Zahn, A., and Ziereis, H.: Dynamics and
 489 composition of the Asian summer monsoon anticyclone, *Atmos. Chem. Phys.*, 18, 5655-
 490 5675, <https://doi.org/10.5194/acp-18-5655-2018>, 2018.

491 Hossaini, R., Chipperfield, M., Montzka, M. P., Rap, S. A., Dhomse, S., and Feng, W.:
 492 Efficiency of short-lived halogens at influencing climate through depletion of stratospheric
 493 ozone, *Nature Geoscience*, 8, 186–190, <https://doi.org/10.1038/ngeo2363>, 2015.

494 Hoskins, B. J., and Rodwell, M. J.: A model of the Asian summer monsoon, I: The global
 495 scale, *J. Atmos. Sci.*, 52, 1329–1340, 1995.

496 Highwood, E. J. and Hoskins, B. J.: The tropical tropopause, *Q. J. Roy. Meteor. Soc.*, 124,
 497 1579–1604, 1998.

498 Houze, R. A., Wilton, D. C., and Smull, B. F.: Monsoon convection in the Himalayan region
 499 as seen by the TRMM 345 Precipitation Radar, *Q. J. Roy. Meteor. Soc.*, 133, 1389-1411,
 500 10.1002/qj.106, 2007.

501 Hu, Y. and Pan, L.: Arctic stratospheric winter warming forced by observed SSTs, *Geophys.*
 502 *Res. Lett.*, 36, L11707, [doi:10.1029/2009GL037832](https://doi.org/10.1029/2009GL037832), 2009.

503 Kishore, P., Ratnam, M. V., Namboothiri, S., Velicogna, I., Basha, G., Jiang, J., Igarashi, K.,
 504 Rao, S., and Sivakumar, V.: Global (50° S–50° N) distribution of water vapor observed by
 505 COSMIC GPS RO: Comparison with GPS radiosonde, NCEP, ERAInterim, and JRA-25
 506 reanalysis data sets, *J. Atmos. Sol.-Terr. Phys.*, 73, 1849–1860,
 507 [doi:10.1016/j.jastp.2011.04.017](https://doi.org/10.1016/j.jastp.2011.04.017), 2011.

508 Kishore, P., Jyothi, S., Basha, G., Rao, S.V.B., Rajeevan, M., Velicogna, I., and Sutterley,
509 T.C.: Precipitation climatology over India: validation with observations and reanalysis
510 datasets and spatial trends. *ClimDyn* 121. doi: [10.1007/s00382-015-2597-y](https://doi.org/10.1007/s00382-015-2597-y), 2015.

511 Kishore, P., Basha, G., VenkatRatnam, M., Velicogna, I., Ouarda, T. B. M. J., and Narayana
512 Rao, D.: Evaluating CMIP5 models using GPS radio occultation COSMIC temperature in
513 UTLS region during 2006–2013: twenty-first century projection and trends, *Clim.*
514 *Dynam.*, 47, 3253–3270, <https://doi.org/10.1007/s00382-016-3024-8>, 2016.

515 Kalnay, E., Kanamitsu, M., Kistler, R., Collins, W., Deaven, D., Gandin, L., Iredell, M.,
516 Saha, D., White, G., Woollen, J., Zhu, Y., Chelliah, M., Ebisuzaki, W., Higgins, W.,
517 Janowiak, J., Mo, K.C., Ropelewski, C., Wang, J., Leetma, A., Reynolds, R., and Dennis,
518 J.: The NCEP/NCAR 40-years reanalysis project. *Bull. Am. Meteorol. Soc.* 77, 437–472.
519 1996.

520 Kursinski, E. R., Hajj, G. A., Schofield, J. T., Linfield, R. P., and Hardy, K. R.: Observing
521 Earth’s atmosphere with radio occultation measurements using the Global Positioning
522 System, *J. Geophys. Res.-Atmos.*, 102, 23429–23465, 1997.

523 Kunze, M., Braesicke, P., Langematz, U., and Stiller, G.: Interannual variability of the boreal
524 summer tropical UTLS in observations and CCMVal-2 simulations, *Atmos. Chem. Phys.*,
525 16, 8695–8714, <https://doi.org/10.5194/acp-16-8695-2016>, 2016.

526 Lau, W.K.M., Cheng, Y., and Li, Z.: Origin, maintenance and variability of the Asian
527 Tropopause Aerosol Layer (ATAL): Roles of monsoon dynamics. *Sci. Rep.* 2018, 8, 3960.

528 McPhaden, M. J., Zebiak, S. E., and Glantz M. H. ENSO as an integrating concept in earth
529 science, *Science*, 314, 1740–1745, 2006.

530 Medina, S., Houze, R. A., Kumar, A., and Niyogi, D.: Summer monsoon convection in the
531 Himalayan region: terrain and land cover effects, *Q. J. Roy. Meteor.Soc.*, 136, 593–616,
532 [10.1002/qj.601](https://doi.org/10.1002/qj.601), 2010.

533 Narendra Reddy, N., Venkat Ratnam, M., Basha, G., and Ravikiran, V.: Cloud vertical
534 structure over a tropical station obtained using long-term high-resolution radiosonde
535 measurements, *Atmos. Chem. Phys.*, 18, 11709–11727, [https://doi.org/10.5194/acp-18-](https://doi.org/10.5194/acp-18-11709-2018)
536 11709-2018, 2018.

537 Pai, D.S., Sridhar, L., and Ramesh Kumar, M.R.: Active and break events of Indian summer
538 monsoon during 1901-2014. *ClimDyn* 46, 3921– 3939. [https://doi.org/10.1007/s00382-](https://doi.org/10.1007/s00382-015-2813-9)
539 015-2813-9, 2016.

540 Pan, L. L., Honomichl, S. B., Kinnison, D. E., Abalos, M., Randel, W. J., Bergman, J. W.,
541 and Bian, J.: Transport of chemical tracers from the boundary layer to stratosphere
542 associated with the dynamics of the Asian summer monsoon, *J. Geophys. Res. Atmos.*,
543 121, 14159-14174, 10.1002/2016JD025616, 2016.

544 Park, M., Randel, W. J., Gettleman, A., Massie, S. T., and Jiang, J. H.: Transport above the
545 Asian summer monsoon anticyclone inferred from Aura Microwave Limb Sounder tracers,
546 *J. Geophys. Res.*, 112, D16309, <https://doi.org/10.1029/2006JD008294>, 2007.

547 Rajeevan, M., Gadgil, S., and Bhate, J.: Active and break spells of the Indian summer
548 monsoon, *J. Earth Syst. Sci.*, 119, 229–247, doi:10.1007/s12040- 010- 0019- 4, 2010.

549 Randel, W. J., and Park, M.: Deep convective influence on the Asian summer monsoon
550 anticyclone and associated tracer variability observed with Atmospheric Infrared Sounder
551 (AIRS), *J. Geophys. Res.*, 111, D12314, <https://doi.org/10.1029/2005JD006490>, 2006

552 Rao, D. N., Ratnam, M. V., Mehta, S., Nath, D., Ghouse Basha, S., Jagannadha Rao, V. V.
553 M., Krishna Murthy, B. V., Tsuda, T., and Nakamura, K.: Validation of the COSMIC
554 radio occultation data over Gadanki (13.48 N, 79.2 E): A tropical region, *Terr. Atmos.*
555 *Ocean. Sci.*, 20, 59–70, doi:10.3319/TAO.2008.01.23.01(F3C), 2009.

556 Ratnam, M. V., Sunilkumar, S., Parameswaran, K., Murthy, B. K., Ramkumar, G., Rajeev,
557 K., Basha, G., Babu, S. R., Muhsin, M., and Mishra, M. K.: Tropical tropopause dynamics

558 (TTD) campaigns over Indian region: An overview, *J. Atmos. Sol.-Terr. Phy.*, 121, 229–
 559 239, 2014.

560 RavindraBabu, S., VenkatRatnam, M., Basha, G., Krishnamurthy, B. V., and
 561 Venkateswararao, B.: Effect of tropical cyclones on the tropical tropopause parameters
 562 observed using COSMIC GPS RO data, *Atmos. Chem. Phys.*, 15, 10239–10249,
 563 doi:10.5194/acp-15-10239-2015, 2015.

564 Ravindrababu, S., Ratnam, M.V., Basha, G., Liou, Y.-A., Reddy, N.N.: Large Anomalies in
 565 the Tropical Upper Troposphere Lower Stratosphere (UTLS) Trace Gases Observed
 566 during the Extreme 2015–16 El Niño Event by Using Satellite Measurements. *Remote*
 567 *Sens.* 2019, 11(6), 687; <https://doi.org/10.3390/rs11060687>, 2019.

568 Riese, M., Ploeger, F., Rap, A., Vogel, B., Konopka, P., Dameris, M., and Forster, P.: Impact
 569 of uncertainties in atmospheric mixing on simulated UTLS composition and related
 570 radiative effects, *J. Geophys. Res.*, 117, D16305, <https://doi.org/10.1029/2012JD017751>,
 571 2012.

572 Santee, M. L., Manney, G. L., Livesey, N. J., Schwartz, M. J., Neu, J. L., and Read, W. G.: A
 573 comprehensive overview of the climatological composition of the Asian summer monsoon
 574 anticyclone based on 10 years of Aura Microwave Limb Sounder measurements, *J.*
 575 *Geophys. Res.-Atmos.*, 122, 5491– 5514, <https://doi.org/10.1002/2016JD026408>, 2017

576 Schreiner, W., Rocken, C., Sokolovskiy, S., Syndergaard, S., and Hunt, D.: Estimates of the
 577 precision of GPS radio occultations from the COSMIC/FORMOSAT-3 mission, *Geophys.*
 578 *Res. Lett.*, 34, L04808, doi:10.1029/2006GL027557, 2007.

579 Sokolovskiy, S. V., Kuo, Y.-H., Rocken, C., Schreiner, W. S., Hunt, D., and Anthes, R. A.:
 580 Monitoring the atmospheric boundary layer by GPS radio occultation signals recorded in
 581 the open-loop mode, *Geophys. Res. Lett.*, 33, L12813, doi:10.1029/2006GL025955, 2006.

582 Solomon, S., Rosenlof, K., Portmann, R., Daniel, J., Davis, S., Sanford, T., and Plattner, G.-
 583 K.: Contributions of stratospheric water vapor to 5 decadal changes in the rate of global
 584 warming, *Science*, 327, 1219–1223, <https://doi.org/10.1126/science.1182488>, 2010
 585 Tissier, A.-S., and Legras, B.: Convective sources of trajectories traversing the tropical
 586 tropopause layer, *Atmos. Chem. Phys.*, 16, 3383–3398, doi:10.5194/acp-16-3383-2016,
 587 2016.
 588 Trenberth, K. E.: Recent observed interdecadal climate changes in the Northern Hemisphere,
 589 *B. Am. Meteorol. Soc.*, 71, 988–993, doi:10.1175/1520-0477(1990)0712.0.CO;2, 1990.
 590 Vernier, J. P., Fairlie, T. D., Natarajan, M., Wienhold, F. G., Bian, J., Martinsson, B. G.,
 591 Crumeyrolle, S., Thomason, L.W., and Bedka, K. M.: Increase in upper tropospheric and
 592 lower stratospheric aerosol levels and its potential connection with Asian pollution, *J.*
 593 *Geophys. Res.*, <https://doi.org/10.1002/2014JD022372>, 2015
 594 Vogel, B., Günther, G., Müller, R., Grooß, J.-U., Afchine, A., Bozem, H., Hoor, P., Krämer,
 595 M., Müller, S., Riese, M., Rolf, C., Spelten, N., Stiller, G. P., Ungermann, J., and Zahn,
 596 A.: Long-range transport pathways of tropospheric source gases originating in Asia into
 597 the northern lower stratosphere during the Asian monsoon season 2012, *Atmos. Chem.*
 598 *Phys.*, 16, 15 301–15 325, <https://doi.org/10.5194/acp-16-15301-2016>, 2016.
 599 Vogel, B., Günther, G., Müller, R., Grooß, J.-U., and Riese, M.: Impact of different Asian
 600 source regions on the composition of the Asian monsoon anticyclone and of the
 601 extratropical lowermost stratosphere, *Atmos. Chem. Phys.*, 15, 13 699–13 716,
 602 <https://doi.org/10.5194/acp15-13699-2015>, [http://www.atmos-chem-](http://www.atmos-chem-phys.net/15/13699/2015/)
 603 [phys.net/15/13699/2015/](http://www.atmos-chem-phys.net/15/13699/2015/), 2015.
 604 Wickert, J., Reigber, C., Beyerle, G., König, R., Marquardt, C., Schmidt, T., Grünwaldt, L.,
 605 Galas, R., Meehan, T. K., Melbourne, W. G., and Hocke, K.: Atmosphere sounding by

606 GPS radio occultation: First results from CHAMP, *Geophys. Res. Lett.*, 28, 3263–3266,
 607 2001.

608 Xie, F., Li, J., Tian, W., Feng, J., and Huo, Y.: Signals of El Niño Modoki in the tropical
 609 tropopause layer and stratosphere, *Atmos. Chem. Phys.*, 12, 5259–5273,
 610 <https://doi.org/10.5194/acp-12-5259-2012>, 2012.

611 Yan, R.-C., Bian, J.-C., and Fan, Q.-J.: The impact of the South Asia high bimodality on the
 612 chemical composition of the upper troposphere and lower stratosphere, *Atmos. Ocean. Sci.*
 613 *Lett.*, 4, 229–234, 2011.

614 Yan, X., Konopka, P., Ploeger, F., Tao, M., Müller, R., Santee, M. L., Bian, J., and Riese, M.:
 615 El Niño Southern Oscillation influence on the Asian summer monsoon anticyclone,
 616 *Atmos. Chem. Phys.*, 18, 8079–8096, <https://doi.org/10.5194/acp-18-8079-2018>, 2018.

617 Yuan, C., Lau, W. K. M., Li, Z., and Cribb, M.: Relationship between Asian monsoon
 618 strength and transport of surface aerosols to the Asian Tropopause Aerosol Layer (ATAL):
 619 interannual variability and decadal changes, *Atmos. Chem. Phys.*, 19, 1901–1913,
 620 <https://doi.org/10.5194/acp-19-1901-2019>, 2019.

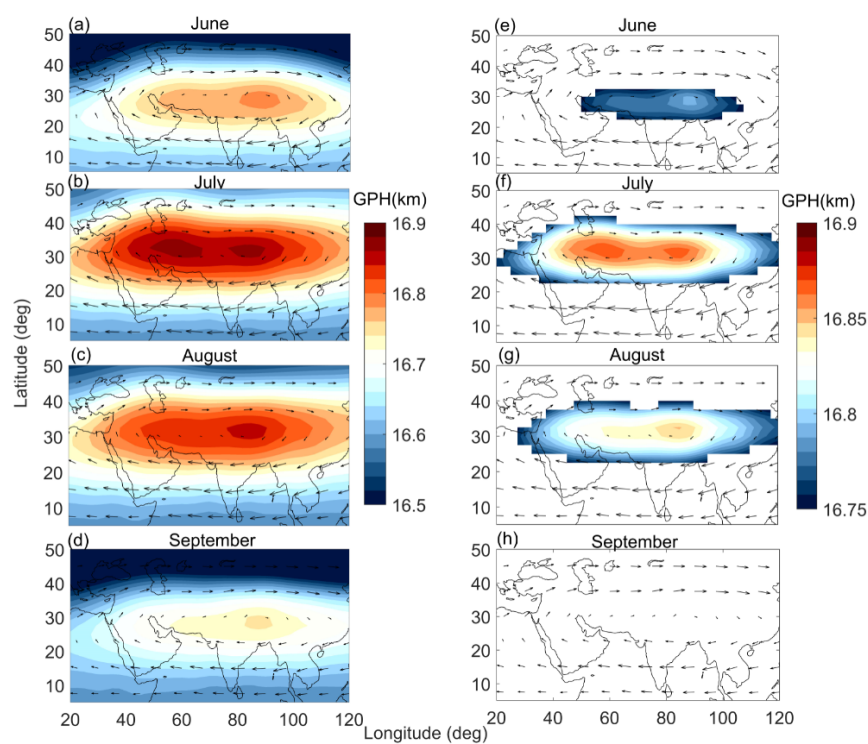
621 Zhang, Q., Wu, G., and Qian, Y.: The Bimodality of the 100 hPa South Asia High and its
 622 Relationship to the Climate Anomaly over East Asia in summer, *J. Meteorol. Soc. Jpn.*,
 623 80, 733–744, 2002.

624 Zubiaurre, I., and Calvo, N.: The El Niño–Southern Oscillation (ENSO) Modoki signal in the
 625 stratosphere, *J. Geophys. Res.*, 117, D04104, doi:10.1029/2011JD016690, 2012.

626
 627

Formatted: Justified, Indent: Left: 0 cm, Hanging: 0.5 cm,
 Line spacing: double

Deleted: .



631
632 Figure 1. Spatial distribution of Geopotential Height (GPH) and wind vectors at 100 hPa
633 during (a) June, (b), July, (c) August and (d) September from NCEP reanalysis data
634 averaged from the year 1951-2016. The core of the anticyclone region was chosen based
635 on the GPH values ranging from 16.75 to 16.9 km. The spatial extent and magnitude of the
636 anticyclone after applying the GPH criteria for (e) June, (f) July, (g) August and (h),
637 September.

638
639
640

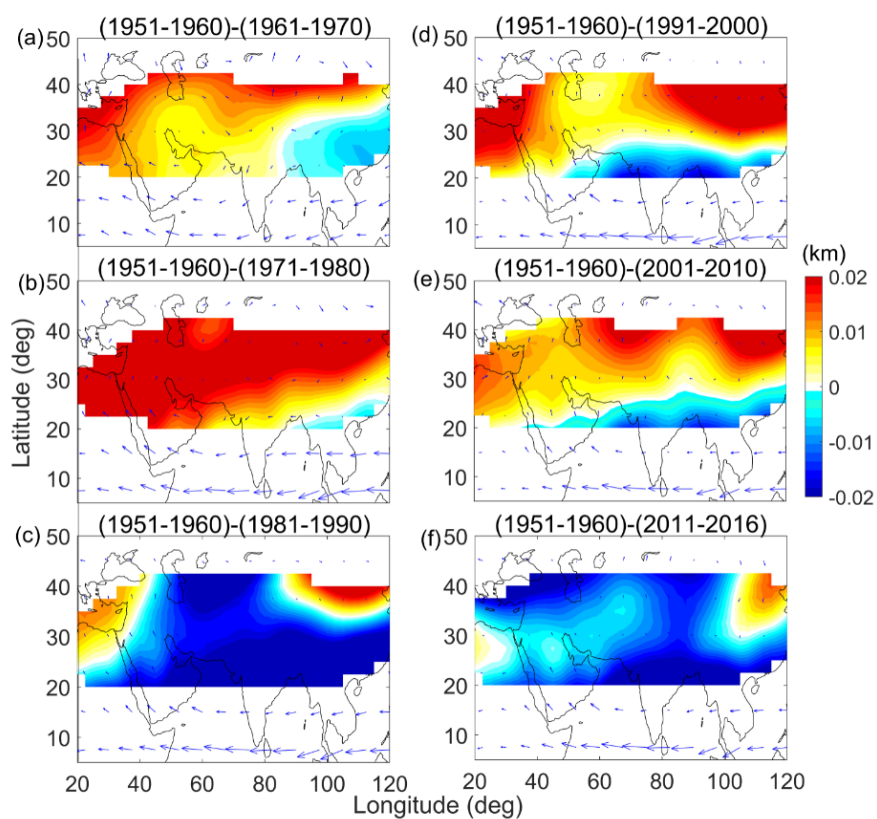


Figure 2. Decadal variation of anticyclone obtained from GPH and wind vectors with reference to 1951-1960 period.

651
652

653
654
655
656
657
658
659

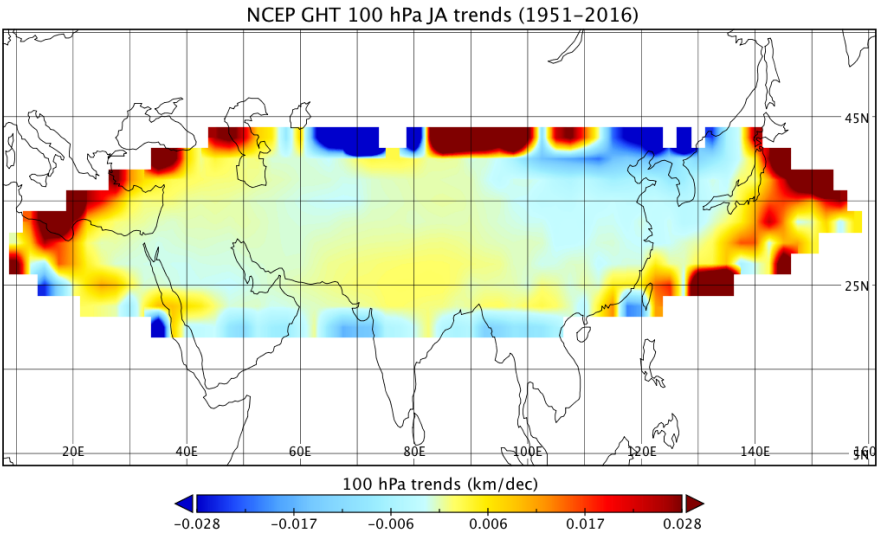
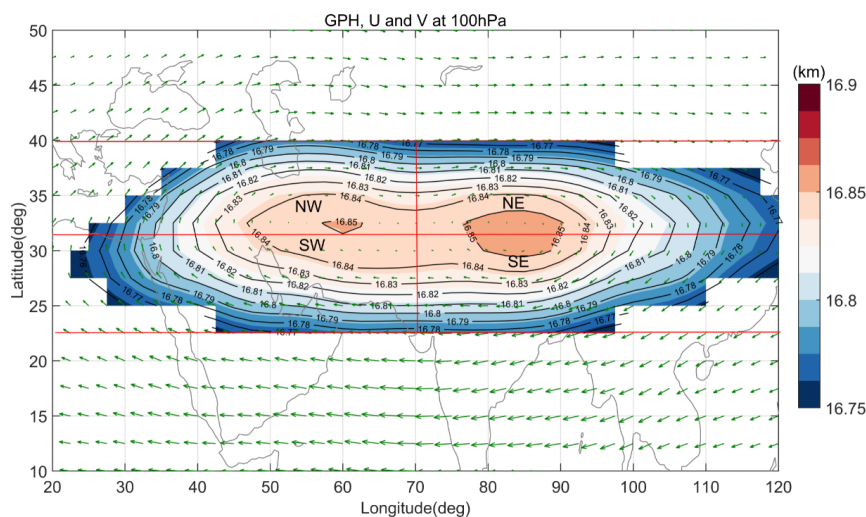


Figure 3. Spatial trend analysis obtained using robust regression analysis at 95% confidence interval.

660



661

662 Figure 4. The climatological distribution of GPH (16.75 to 16.9 km) and wind vectors
663 averaged during July and August from NCEP reanalysis data along with contour lines at
664 100 hPa from 1951-2016. The anticyclone region is further divided into 4 sectors based
665 on peak values of GPH. The GPH values peak centres at 32.5°N in latitude and 70°E in
666 longitude. The sectors are further divided into South-East (SE) (22.5°N-32.5°N), North-
667 East (NE) (32.5°N-40°N) in longitude band 70°E-120°E, South-West (SW) (22.5°N-
668 32.5°N), and North-West (NW) (32.5°N-40°N) at 20°E-70°E longitude range.

669

670

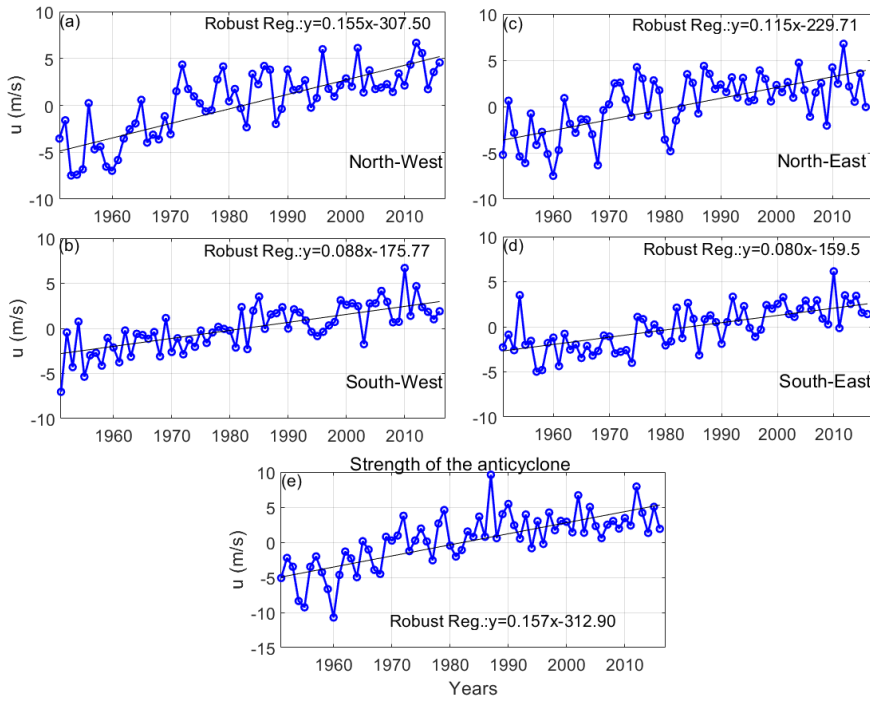
671

672

673

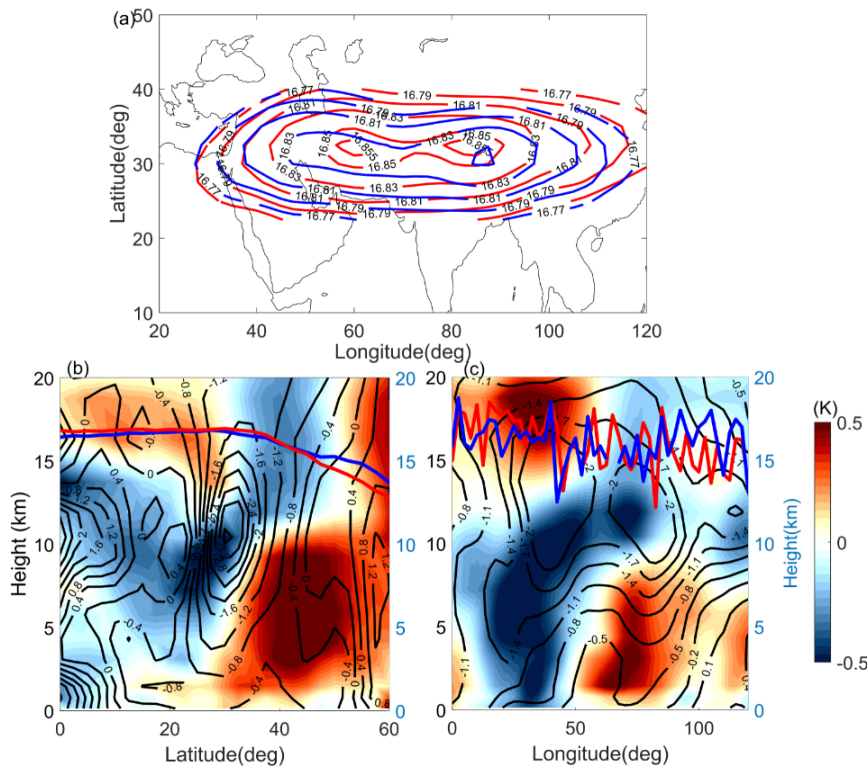
674

675



676

677 Figure 5. Time series of zonal wind anomalies estimated for (a) North-West, (b) South-West,
 678 (c) North-East and (d) South-East sectors of ASMA. The trend analysis was performed at
 679 95% confidence interval by using robust regression analysis. (e) The strength of the
 680 anticyclone was estimated from the zonal wind difference between (30°N-40°N)-(10°N-
 681 20°N) in the longitude band of 50°E-90°E.

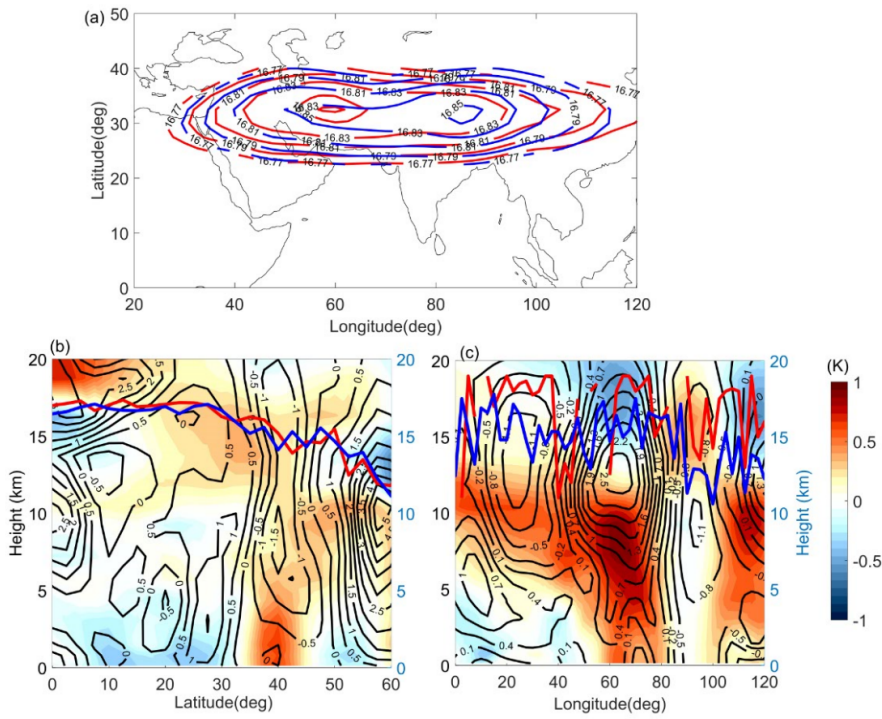


682

683 Figure 6. (a) ASMA variability during active and break phases of Indian monsoon obtained
 684 from GPH at 100 hPa. Red line indicates the active and blue line for break phase of Indian
 685 monsoon. (b) Latitude-altitude cross-section of temperature (colour shaded, K) and zonal
 686 wind anomalies (contour lines, m/s) which are estimated from difference between active
 687 and break phases of Indian Monsoon in the longitude band of 80°E-90°E. (c) Longitude-
 688 altitude cross-section of temperature and wind anomalies averaged between 30°N-40°N.
 689 The red and blue lines in Figure 6b & 6c denotes the tropopause altitude during active and
 690 break spells of Indian monsoon estimated using GNSS RO data, respectively.

691

692

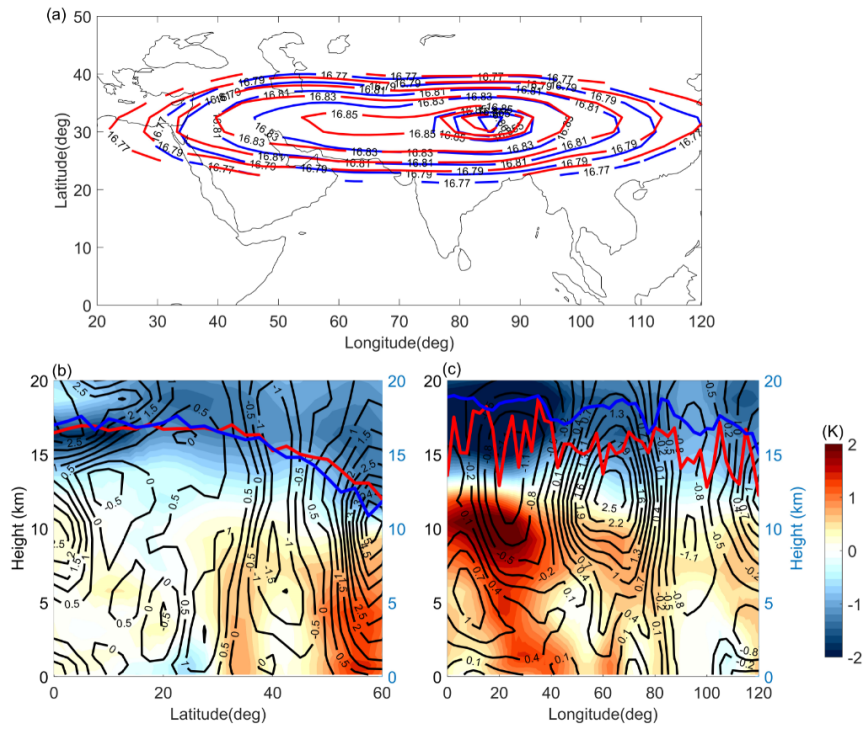


693

694

695 Figure 7. (a) ASMA variability obtained from GPH at 100hPa during strong and weak
 696 monsoon years calculated based on high resolution rainfall data in band of 5°N-30°N,
 697 70°N-95°E grid. Red line indicates the strong and blue line for weak monsoon years. (b)
 698 Latitude-altitude cross-section of temperature (colour shaded, K) and zonal wind
 699 anomalies (contour lines, m/s) which are estimated from difference between strong and
 700 weak monsoon years in the longitude band of 80°E-90°E. (c) Longitude-altitude cross-
 701 section of temperature and wind anomalies averaged between 30°N-40°N. Red and blue
 702 lines in Figure 7b & 7c denote the tropopause altitude during strong and weak monsoon
 703 years estimated using GNSS RO data, respectively.

704



706

707 Figure 8. (a) ASMA variability obtained from GPH at 100 hPa during strong La Niña and El
708 Niño years. Red and blue lines indicate the La Niña and El Niño years. (b) Latitude-
709 altitude cross-section of temperature (colour shaded, K) and zonal wind anomalies
710 (contour lines, m/s) which are estimated from difference between La Niña and El Niño
711 years in the longitude band of 80°E-90°E. (c) Longitude-altitude cross-section of
712 temperature and zonal wind anomalies averaged between 30°N-40°N. The red and blue
713 lines in Figure 8b & 8c denote the tropopause altitude during La Niña and El Niño years
714 estimated from GNSS RO data, respectively.

715

716